Theoretical and Applied Fracture Mechanics 122 (2022) 103552

Contents lists available at ScienceDirect

Theoretical and Applied Fracture Mechanics

journal homepage: www.elsevier.com/locate/tafmec

On different 3D printing methods and fracture performance in DCB composite specimens including structured interfaces

M.T. Aranda *, J. Reinoso, I.G. García

Departamento de Mecánica de Medios Continuos y Teoría de Estructuras, Escuela Técnica Superior de Ingeniería, Universidad de Sevilla, Camino de los Descubrimientos s/n, 41092 Sevilla, Spain

ARTICLE INFO

Keywords:
Biomimetic interfaces
Structured interfaces
3D printing
Fracture toughness
Composite materials

ABSTRACT

This work experimentally analyzes the influence of the printing direction on the fracture resistance capabilities of composite specimens incorporating structured interfaces in their geometrical definition. In particular, we compare horizontal and vertical direction fiber deposition using 3D printing capabilities in order to identify the best scenarios that maximize the corresponding fracture performances. For this purpose, DCB specimens including improved structured interfaces designed with fiber in the profile region of the specimen are produced. These designs were created using 3D printing in long fiber composites. Experimental evidences reveal a remarkable increase in fracture toughness in structured interface profiles printed in the vertical direction compared to structured interface profiles printed in the horizontal direction, specifically 217% for the best configuration and 118% for the most unfavorable configuration. Present results show the potential benefits for the generation of novel design concepts with improvements in fracture resistance capabilities, fostering new perspectives in the definition of composite structures.

1. Introduction

Natural resources such as bone, wood, and shells aided the technological development of humanity in its early stages. As history advanced, these materials were gradually replaced with synthetic compounds with improved mechanical performances. Nowadays, scientists are inspired by the distinctive qualities of the complex designs of natural structures, which can be lightweight and offer combinations of mechanical properties that often overcome those of their components. Hence, natural organisms provide a rich source of inspiration for novel ideas. They allow us to benefit from the vast number and diversity of solutions that have been perfected over millions of years of evolution. Specifically, they arrest crack propagation and prevent catastrophic failure [1–4]. Although mimicking the properties of natural material is a complex process, the first steps in characterization, modeling, and manufacturing have been taken. Such progress is encouraging the growing conviction that highly damage-tolerant bioinspired structures can be designed and manufactured [5].

For instance, biological structural materials often combine stiff and soft components in hierarchical structures (Fig. 1(a)). In particular, in this search for optimization of the response of different engineering components, the study of the material of nacre can be highlighted [6,7], where interfaces with complex geometries provide a preferred path for crack deflection, thus contributing to the increase in fracture resistance (Fig. 1(b)).

In this respect, a prospective route for further research would comprise the exploitation of so-called structured interfaces. In particular, this concept is referred to the idea of non-planar interfaces with structural patterns (structured interfaces) in contrast to standard flat interfaces. This idea generally stems from nature observation, so they are also known as biomimetic interfaces [8,9].

Additive manufacturing is a promising new technology to meet this challenge since provides a fast, accurate, and repeatable way to fabricate the biomimetic designs, (Fig. 1(c)). As an example of the high impact and applicability of these concepts, in the recent literature, find bio-inspired designs with 3D printing: interlocking suture materials including the friction and contact [15], bone-shaped 3D structures with a “brick and structure mortar” that creates high fracture toughness [16,17], mechanics of suture-shaped joints that connect more rigid components (containing triangular, rectangular, trapezoidal, etc.), hierarchical and fractal interfaces, the influence of the geometry of the shape of wave and its length parameters (such as amplitude and wavelength, among others) [12,18,19]. In this context, the works of Zavattieri using interface designs are remarkable. Sinusoidal in adhesive joints [18] by using cohesive elements to predict the fracture mechanism or the development of fracture processes in helical or

* Corresponding author.
E-mail address: maranda2@us.es (M.T. Aranda).

https://doi.org/10.1016/j.tafmec.2022.103552
Received 23 May 2022; Received in revised form 28 July 2022; Accepted 22 August 2022
Available online 8 September 2022

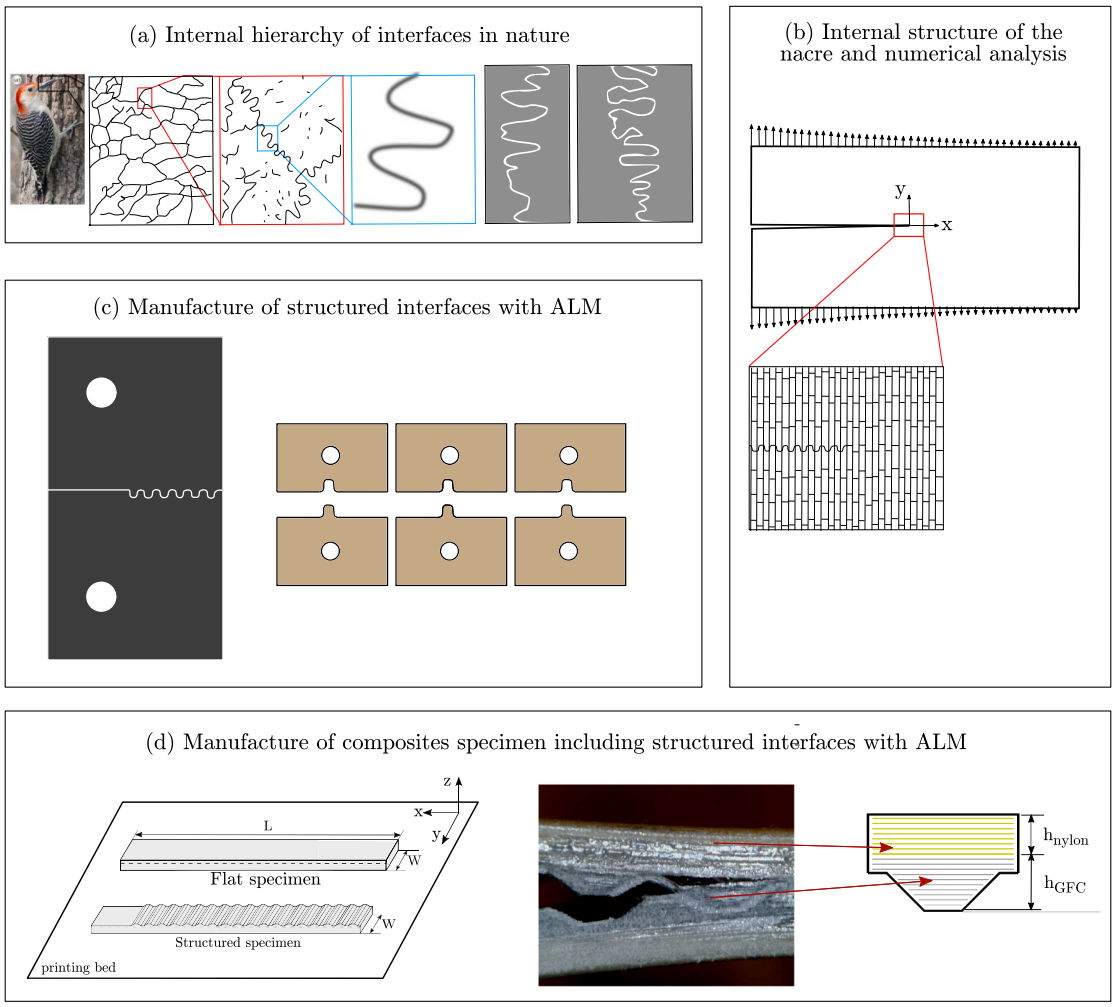

Fig. 1. (a) Transmission electron microscope cross-section image of the woodpecker's beak at different length scales (Adapted from [10]), (b) Internal structure of the nacre and numerical analysis (Adapted from [7]) and (c) A jig-saw-like interface laser engraved glass specimen (Adapted from [11]), sinusoidal DCB interface in a metal specimen (Adapted from [12]) and 3D printed samples with interlocking suture (Adapted from [13]). (d) Illustration of an undesirable response attributed to the printing process. Crack growth migrates to the adjacent region of the specimens. Schematic of material used into the profile, showing the incapability of employing fibers into the structured profile [14].

Bouligand structures. Lastly, as this proposal is more geared towards technology transfer, it is mentionable that many of these investigations have given rise to numerous patents that are capable of being industrially implemented and commercialized [20]. However, the vast majority of these works have been fundamentally oriented towards the analysis of metallic alloys [12,21] or polymeric materials such as nylon fibers [22] and ABS materials [23–25].

Within the context of composite materials, only a very limited number of investigations have focused on the production of composite components, including specimens with biomimetic interfaces. Specifically, as has been amply reported in the related literature, composites exhibit excellent capacities in terms of specific stiffness and resistance. This has promoted that their incorporation in different engineering applications has experimented an extraordinary increase in the last decades. Composite materials have been used extensively in strategic and highly technological sectors such as aeronautical, space, automotive, and energy (with particular prevalence in the development of renewable energies). Motivated by this technological impact, continuous research efforts have been performed for the development of increasingly efficient structures, minimizing the required structural weights and consequently reducing the corresponding ecological impact in terms of fuel consumption or optimizing the structural response to the appearance of damage phenomena.

In fact, the interfaces are mainly designed for shear load transfer and have been analyzed by different authors, see e.g. [26–29]. However, the interface could transfer tensile load in certain joint configurations, such as the run-out in the aeronautical sector. In these regions of stringer-skin joints, the interface is mainly subjected to tensile load, thus the design has to focus on avoiding peeling and debonding risks for these aircraft components, see e.g. [30–35].

From a manufacturing perspective, current processes for the production of composite structures of long fibers are mainly limited in their dimensions and in their global automation for the use of the autoclave in its curing process. Although there have been advances aimed at eliminating the autoclave as a necessary element through various techniques [36,37], currently its use is widespread.

In light of the previous arguments, the principal idea behind the use of structured interfaces introduced in this section might foster a new paradigm in the conception of the structural joints in engineering composite structures. Furthermore, these developments might lead to the proper exploitation of the load bearing capabilities mentioned above, with significant economic, environmental and societal impact.

Research activities on this matter have been originally carried out at the Group of Elasticity and Strength of Materials (GERM) of the Universidad de Sevilla (US) in the use of manufacturing procedures based on 3D printing techniques. A first action in this direction was performed by Justo et al. [38], where an exhaustive characterization analysis of the different mechanical properties in terms of stiffness and resistance of various specimens manufactured by such procedures was

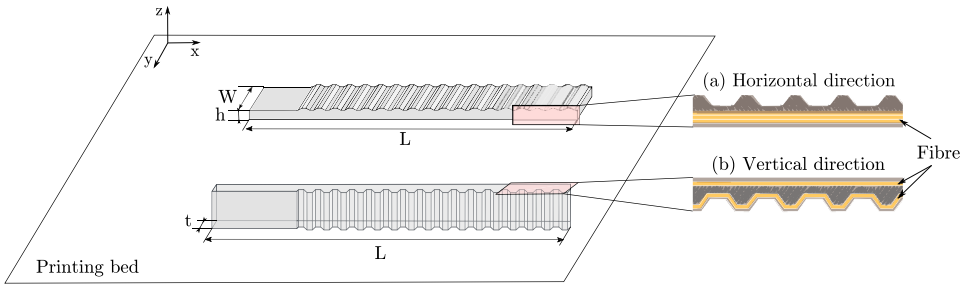

Fig. 2. Comparison of printing direction for specimens including structured interfaces which could provide a preferred crack path. (a) Schematic of the specimen manufactured in horizontal direction defined in [14]. (b) Schematic of the specimen under study designed in vertical direction. Improved design with fiber around the structured profile.

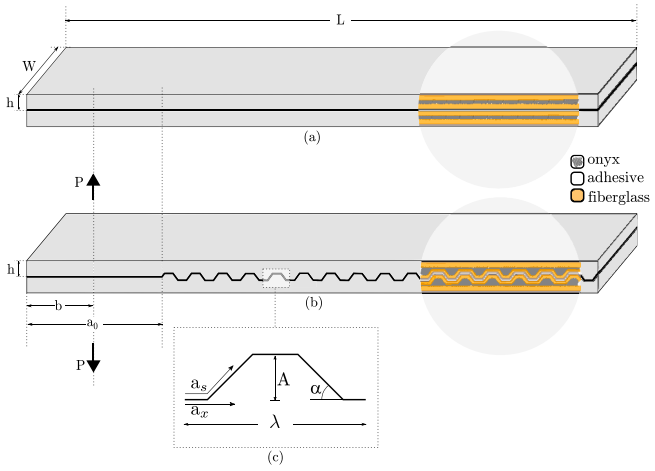

Fig. 3. (a) Double cantilever beam (DCB) with a flat interface of length L, thickness h, width W and pre-crack length a_0. (b) DCB with trapezoidal interface of parameters A, amplitude, and l, wavelength. Distance between the left end of the beam and the applied displacement point is represented by b. (c) Magnified view of trapezoidal interface. The actual crack length measured from the initial point (0;0) is a_s. The projection of the crack length a_s along the x-axis is a_x and the angle of the leaning section is $\alpha = \tan^{-1}\frac{4A}{\alpha}$. (d) Zoom view of material used.

carried out. Justo et al. [38] showed that in the current state of the art, specimens obtained by 3D printing are not competitive, in relation to their mechanical properties with those produced in an autoclave, thus inviting significant improvements in current technical capabilities.

Subsequently, a detailed research from experimental, analytical and numerical points of view in relation to the mechanical behavior of composite specimens manufactured with 3D printing including structured interfaces with trapezoidal patterns (see Fig. 1(d)) was performed by García-Guzmán et al. [14]. Promising perspectives emanate from this study, where every structured configuration increased the fracture energy with respect to the reference straight interface in the debonding process, see Fig. 1(d). Special attention was given to various aspects that emerged of crucial importance, such as:

(i) the definition of a reliable fabrication procedure for the fabrication of DCB specimens of composite materials for subsequent testing, including structured interfaces.
(ii) the identification of the geometric definition of such interfaces, which corresponds to the most advantageous scenario in terms of fracture resistance, using the A/λ (amplitude/wavelength of the structured pattern), see Fig. 3.

However, relying on the main conclusions drawn by García-Guzmán et al. [14], Additive Layer Manufacturing (ALM) production capabilities showed notable manufacturing drawbacks. The most important aspect was related to the impossibility of using fibers into the structured profile region of the specimen due to the printing direction parameter, see Fig. 1(d). This limitation could induce less fracture toughness in such regions and on some occasions cause undesirable results, e.g. crack growth could migrate from the interface to the bulk, not being confined to adjacent regions of the specimens.

Motivated by these real scenarios, this study aims to improve the current design proposed by García-Guzmán et al. [14]. It is particularly relevant for the ALM technique to evaluate the influence of the printing direction parameter on the fracture resistance capabilities. The comparison between these two configurations (see Fig. 2) will allow to identify the best 3D printing scenarios.

Currently, how the processing parameters, such as printing directions, influence the quality of the printed products has received very scarce attention [17,39]. In order to explore the influence of these processing parameters, an experimental campaign based on digital image correlation (DIC) is carried out, evaluating the capability of structured interfaces to address the crack path.

In the sequel, the organization of the article is as follows. In Section 2, the specimens design and fabrication procedure are described. The experimental campaign will be presented in Section 3, including a description of the experimental setup, a detailed analysis of the results and their corresponding interpretation. The experimental comparison of fracture capabilities in structured interface printing in vertical direction respect to horizontal direction will be addressed in Section 4. Finally, the main conclusions are summarized in Section 5.

2. Specimen design and fabrication

The main goal of this study concerns the exploration of alternative designs for specimens including interfaces with structural profiles (Fig. 2). For that purpose, this section discusses the design considerations regarding the definition of specimens in the vertical direction, which will then be compared to specimens manufactured in the horizontal direction as established by García-Guzmán et al. [14].

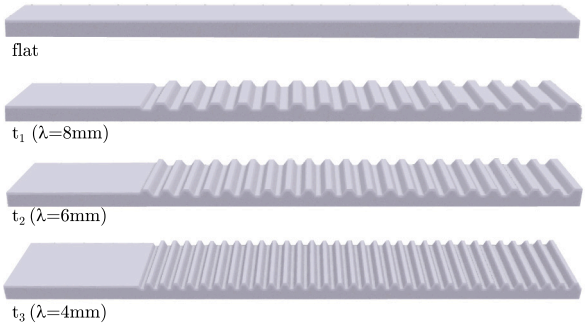

Fig. 4. 3D view of types of specimen design studied with the different interface configurations: (a) flat interface, (b) structured interface, t_1 (λ = 8 mm, A = 2 mm), (c) structured interface, t_2 (λ = 6 mm, A = 2 mm) and structure interface t_3 (λ = 4 mm, A = 2 mm).

According to the specifications [40,41], a schematic definition of the bonded double cantilever beam (DCB) specimen employed in this study is represented in Fig. 3(a) for flat interfaces and Fig. 3(b) for structured interfaces. Both specimen types consisted of two laminates bonded by an intermediate very thin adhesive layer with identical overall dimensions: length, L = 169 mm, width, W = 25 mm, thickness, t = 4.8 mm, and the same initial crack tip position, which is located at a distance, a_0 = 40 mm, from the left side of the beams where the load is applied. Note that the beam thickness, t, used in the experiments are limited to the minimum thickness for which it is possible to print fibers around the contour of the structured interfaces.

Fig. 2(b) shows the direction under study, which was set with the material deposition along the width direction of the specimen (referred to as printing in vertical direction), which located the longitudinal axis (L) and the thickness axis (t) of the specimen on the printing bed.

The main advantage of setting the vertical direction as the printing direction is that the structured profile could be manufactured using fiberglass, i.e. the reinforced fiber may reach the contour of the structured interface (Fig. 2(b)). This led to an innovative design of structured interfaces of in DCB-type composite specimens in comparison to those described in [14] where reinforcing fibers could not reach the region of the structured profile (Fig. 2(a)). These limitations stemmed from the specifications of the 3D printing system, requiring a minimum area equal to 6.45 cm^2 to use fiber-reinforced material within a layer during the manufacturing process. The layers of the trapezoidal interface consisted of small rectangles whose areas were smaller than this threshold value.

Details of the structured interface are shown in Fig. 3(c). Among the differing patterning options, García-Guzmán et al. [14] showed that trapezoidal profiles can provide an excellent compromise between fracture resistance and geometric tolerance using the production capabilities aforementioned. Consequently, the geometric considerations of the patterned interfaces were designed following the guidelines of the best scenarios discussed by García-Guzmán et al. [14] setting: three different wavelengths (λ = 4,6,8 mm) and an amplitude of the pattern (A = 2 mm) were determined. This leads to the structured configurations: i) t_1 (λ = 8 mm, A = 2 mm), t_2 (λ = 6 mm, A = 2 mm) and t_3 (λ = 4 mm, A = 2 mm). A sketch of the different designs used is presented in Fig. 4. The identical overall dimensions were employed with flat interface specimens, in order to guarantee a similar bending stiffness with respect to the patterned specimens.

Another improvement of the new design was the generation of the initial crack. The precrack in [14] was previously produced as a notch during the printing, resulting in artificially higher values of peak load. In order to avoid some of these defects and to guarantee an initial crack length (a_0) in line with standard DCB specimens, a non-adhesive film was inserted along the first 40 mm of each beam during the joining process, generating a non-adhesion zone (Fig. 16). This film was 20 μm in thickness approximately, preventing this zone from being adhered to the epoxy and thus generating a crack once the epoxy was cured. As a result, some defects found in [14] were avoided.

Table 1
Measurements of Width, length and thickness for the produced DCB specimens with trapezoidal interface profiles employed in the experimental campaign.

Name	W_1	W_2	W_3	t_1	t_2	t_3	L
p_1	25.17	25.1	25.1	10.2	10.1	10.17	169.6
p_2	25.05	25.05	25.01	9.55	9.45	9.71	169.52
p_3	25	25.1	25.1	9.9	9.9	9.9	169.6
p_4	25.12	25.19	25.02	10.15	10.07	10.2	169.5
p_5	25.15	25	24.98	10.07	9.91	9.75	169.3
t_{1-1}	25	25.1	25.1	9.92	10.1	10.1	169.5
t_{1-2}	25.02	25.1	24.94	10	9.99	10	169
t_{1-3}	25.2	25.3	25.4	10.1	10.4	10.6	169.6
t_{1-4}	24.97	24.96	24.99	10.1	10.05	10.2	169.57
t_{1-5}	25.1	25.1	25.1	10.2	10.3	10.44	169.4
t_{1-6}	25.1	25.08	25	10.3	10.2	10.3	169.3
t_{2-1}	25	25	25.1	10.15	10.7	10.77	169.7
t_{2-2}	25.1	25.06	25	10.18	10.3	10.3	169.5
t_{2-3}	24.94	25.17	25.1	9.61	10	10.1	169.5
t_{2-4}	25	25	25.1	10.1	10.2	10.44	169.5
t_{2-5}	25.09	25.1	25	10.8	10.44	10.29	169.4
t_{3-1}	25.17	25.12	25.2	10.23	10.49	10.43	169.9
t_{3-2}	25.15	25.24	25.1	9.9	10	10.2	169.4
t_{3-3}	25.1	25.1	25.1	10.1	10	10	169.3
t_{3-4}	25.1	25.1	25.1	10.1	10.1	10.1	169.4
t_{3-5}	25.2	25.08	25.1	9.72	10.17	9.94	169.39

The specimens with flat and wavy interface were manufactured via additive manufacturing (AM) using the 3D printing equipment (MarkTwo® 3D-printer) which includes the CAD software Eiger® for the definition of the solid model.

The composite printer employs Filament Fusion Fabrication (FFF) technology through two printing media: (i) Composite Base filament onyx (composed of micro carbon fiber filled nylon) and (ii) Continuous Fiber Reinforcement (CFR). Particularly, the production of hybrid onyx–fiberglass specimens were considered. The nozzle temperature used for onyx and fiberglass was 265 °C and 255 °C, respectively.

The objectives regarding the use of fiberglass for the current prototypes were twofold: (i) taking advantage of the superior strength and stiffness properties of fiberglass over onyx from a mechanical point of view, (ii) the idealization of a robust design and printing process that allowed the production of DCB coupons incorporating structured interfaces to be carried out within acceptable geometrical tolerances. The mechanical properties of onyx material herein employed are: Elastic modulus E = 2.4 GPa and Poisson's ratio ν = 0.34 and for the fiberglass reinforced material are: E_{11} = 25.84 GPa; E_{22} = 1.13 GPa; ν_{12} = 0.37; G_{12} = 0.88 GPa (obtained experimentally by Justo et al. [38] and Mudarra Acebedo [42] for a laminated direction of 0°.).

Each of the beams that composed the DCB system consisted of 250 layers with 0.1 mm in thickness. The production of hybrid onyx–fiberglass is considered in every layer in the positions illustrated in Fig. 2. The first and last layers of the vertical print were totally produced using onyx to ensure a good surface finish of the external surface of the samples.

After machining the specimens, the dimensions and standard deviation values were checked. In this way, the thickness and width of each specimen were carefully measured. Thickness and width were the mean values obtained from three points selected to be representative of the specimen, according to the tolerances recommended in [41], (see Table 1).

In addition, measurements using the TR100 surface roughness tester revealed an initial arithmetic mean roughness of R_a around 6-8 μm across all the specimens.

The two sides of the DCB coupons for each configuration (flat or structured) were manufactured and cleaned in order to eliminate any additional debris and contaminants. Subsequently, the final system

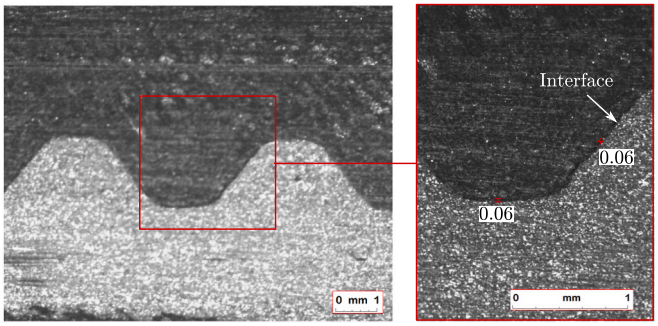

Fig. 5. Example of observations through a microscope to measure the adhesive thickness of the specimen.

was assembled. For this purpose, the two beams of each DCB coupon were bonded with the adhesive at room temperature. The mechanical properties of the adhesive are: ultimate strength $\sigma_u = 31.5$ MPa, rupture strain $\epsilon_f = 1.76\%$, Elastic modulus $E = 4.1$ GPa. These properties were obtained when the adhesive was strained at 0.1 min^{-1} after being cured for 45 min at 75 °C [43].

The two beams were joined together using zip ties in the middle and on both sides of the specimen, via the induction of low pressure and the proper adhesive thickness. Finally, the samples were cured at room temperature (controlled) for a period of 6 days.

The samples were also carefully examined with the aim of determining the adhesive thickness. This thickness ranges from 0.05 mm to 0.1 mm, the smallest thickness corresponding to the oblique region of the structured profile, whereas the largest values correspond to the horizontal sections. This was due to the structured profile of each beam does not fit each other completely. Future developments are planned to improve this aspect (see Fig. 5).

According to AITM1-0053 [40] and ISO Central Secretary [41] five samples of each configuration were produced. In total, twenty specimens were manufactured with the structured profiles described above.

3. Experimental campaign

3.1. Experimental set-up

In this section, the set-up of the experimental campaign and a detailed description of the tests are outlined. The experimental set-up, as shown in Fig. 6, consisted of: (i) a mechanical system to apply tensile loading on the DCB specimen, and (ii) a DIC system to record the specimen during crack growth.

Tests were performed using a universal testing machine INSTRON 4482, with a load cell of 5 kN under displacement-control conditions. The loading application was carried out by the adoption of a uniform applied displacement of 1 mm/min during the tests. The current experimental program was executed in an environmentally controlled room at 22 °C and 1 atm.

Prior to the conduction of the test, auxiliary guiding lines for crack location were marked on both sides of the specimen for the initial and final crack lengths, $a_i = 50$ mm and $a_{i+n} = 110$ mm, see Fig. 6.

To avoid any influence of the incorporated non-adhesive film, the specimen was preloaded until the crack length exceeds approximately 10 mm from the initial length of the non-adhered region. The crack tip (a_i) was then equal to 50 mm from the beginning of the specimen. Then, the sample was completely unloaded. This corresponds to the first loading–unloading in Fig. 7.

The position of the crack tip of the precrack on both edges of the specimen was marked and then the specimen was reloaded at a rate of 1 mm/min till the crack reaches the final length mark, $a_{i+n} = 110$ mm. Crack length was monitored during the whole test.

After the reloading of specimens, the load decreases as the crack starts to propagate along the interface. The energy released in each configuration is represented by the enclosed area between the part of the curve corresponding to crack growing and the straight lines joining this curve with the origin, these straight lines representing the hypothetical unloading curves, see Fig. 7.

The digital image correlation (DIC) technique was also employed during each test to track position of the crack tip. A random speckle pattern was sprayed over the specimen surface, and the corresponding images were acquired before and after the fracture event.

Fig. 8 shows the map of the displacement at different stage of the structured (t_{1-1}) interfaces in comparison with the results for flat interfaces. The displacements (Y) were identical between the two configurations until the first stage, when the fracture reaches the first mark. During the second stage, the displacement of the structured interface is more than double of the flat interface. In contrast, as can be observed from the time parameter, the fracture grows more slowly in the structured interface scenario, at around half the rate of the flat interface specimen, due to the complex profile.

Fig. 9 depicts the strain map at various stages for structured (t_1 – 1) and flat interfaces. Before the propagation it can be observed a continuity in strain field across the interfaces, which indicates perfect bonding. Once the crack starts to propagate, it is possible to observe where a discontinuity in the vertical strain field occurred, which allows detecting the crack tip positions in each moment. As can be seen, there is not a significant variation in strain across the specimen in the two configurations.

3.2. Experimental results

This section describes the experimental results using the new design of interfaces and the comparison between 3D printed onyx–fiberglass reinforced DCB specimens with flat and trapezoidal interface profiles.

The experimental load–displacement curves for four structured patterns with different aspect ratios, amplitude/wavelength = 2/8, 2/6, 2/4, 0 (flat) are displayed in Fig. 10. For each interface geometry, five specimens were tested. The curves for structured specimens exhibit similar characteristics to those observed for flat DCBs. It was noticed that the initial slopes for each design were quite close to each other, indicating that such arrangements had similar bending stiffness. It was also observed that the load–displacement curves for structured geometric show periodic “serrations” which are less noticeable for $A/\lambda = 1/4$.

Fig. 11 shows some representative load–displacement curves with the aim to compare the general trend of each configuration. We note that the bending stiffness in the flat specimen curves results higher than that of the structured specimens. For the different cases of structured geometries, the bending stiffness result identical. It also distinguished that critic load value, P_c, increases with increasing A/λ.

To provide a more performed insight of the crack propagation phases during the tests, Fig. 12 depicts one representative load–displacement curve and the DIC images at different phases for a structured interface $\lambda = 8$ mm. This evolution curve is distinguished by periodic crests with positive and negative slope regions. A similar behavior is observed for sinusoidal interfaces metallic alloys in [12]. The sketch of the pattern in Fig. 12 shows schematic of the structured interfaces with the periods of slow (red) and fast (blue) crack propagation. In fact, the positive slope regions during the evolution correspond to the stable crack growth along the positive inclined sections (red) and followed by an unstable crack growth (blue) featuring to a drop in the load value of the curve. This means that when the crack reaches the crest, this begins to grow at a much higher rate with respect to the applied displacement, decreasing the load. The crack propagation then slows down, which corresponds to the next crest, and the load begins to increase again following again the cycle.

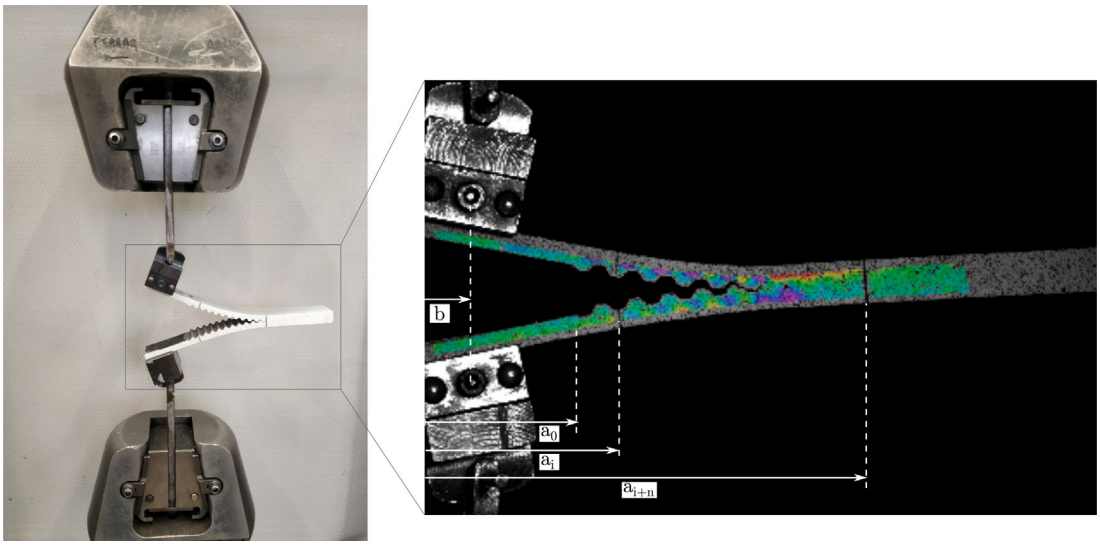

Fig. 6. Close-up photograph of the experimental setup under study. Trapezoidal interface specimen (A/λ = 2/8 mm) with load blocks. Black marks in the specimen indicate the projection of the actual crack length along the x-axis in the position a_{x1} = 50 mm and a_{x2} = 110 mm. Specimens were prepared using the DIC procedure, which included spotting with black and white sprays. Due to the thickness of the specimen, the speckle patterns were very small and are not visible in the photo.

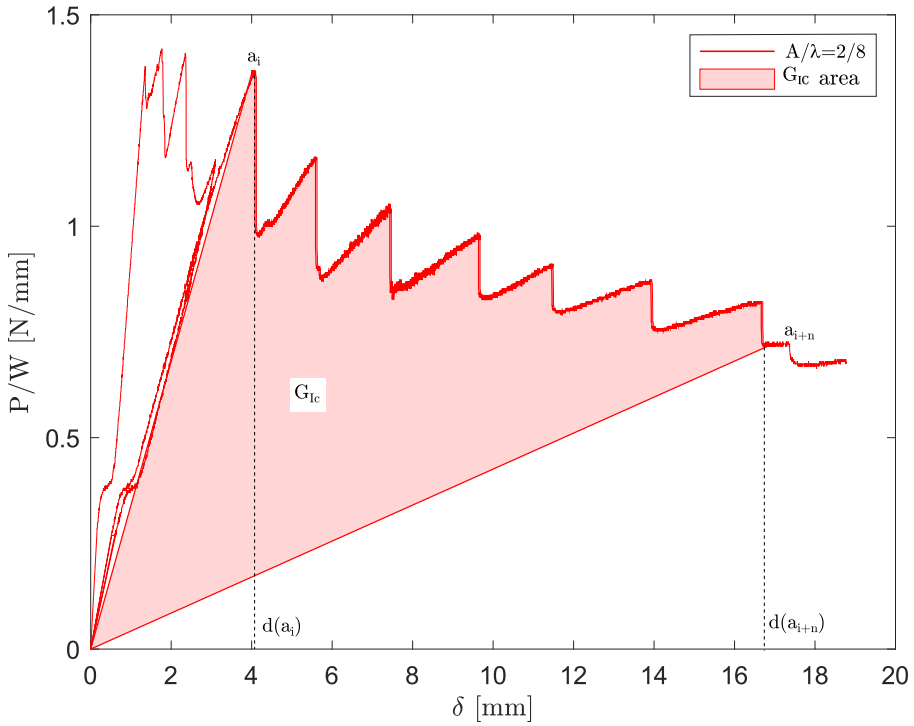

Fig. 7. Load–displacement curve for structured interface t_1 (A= 2 mm; λ = 8 mm). The filled area represents the energy released during the DCB tests between effective crack lengths of a_{x1} = 10 mm and a_{x2} = 70 mm.

A comparable crack propagation behavior is observed in the other types of configurations, A/λ = 2/6 and 2/4, as depicted in Figs. 13 and 14, respectively. The structured DCBs induce intermittent crack extension that resemble specific portions of the structured interfaces with stable-unstable behavior. However, it is observed in these types of configurations that the evolution of stable crack growth advances a larger profile distance with increasing Aλ.

The quantification of bonded joint fracture toughness energy for each specimen was carried out by processing the data from the load–displacement curve. In this case, we assumed that this evaluation could be obtained using standard methods that have been widely used on flat DCBs [40,41]. It should be noted that AITM1-0053 [40] was used instead of ISO Central Secretary [41]. The ISO standard bases its calculations on stiffness (analyzing the specimen as a beam), whereas AITM bases its estimates on the area under the curve to calculate the fracture toughness in mode I. The load–displacement curve of a structured interface is characterized by the corresponding peaks (i.e., the crack propagates quickly and it is followed by crack arrests that correspond to small drops in the load value). For this reason, AITM1-0053 [40] is preferable as it would be able to take into account the area under those peaks. In addition, the ISO standard makes some hypotheses to calculate the stiffness, as uniform beam section, which could be not applicable to specimens with structured interfaces. Thus, the AITM standard will be used here and the fracture toughness in Mode I is

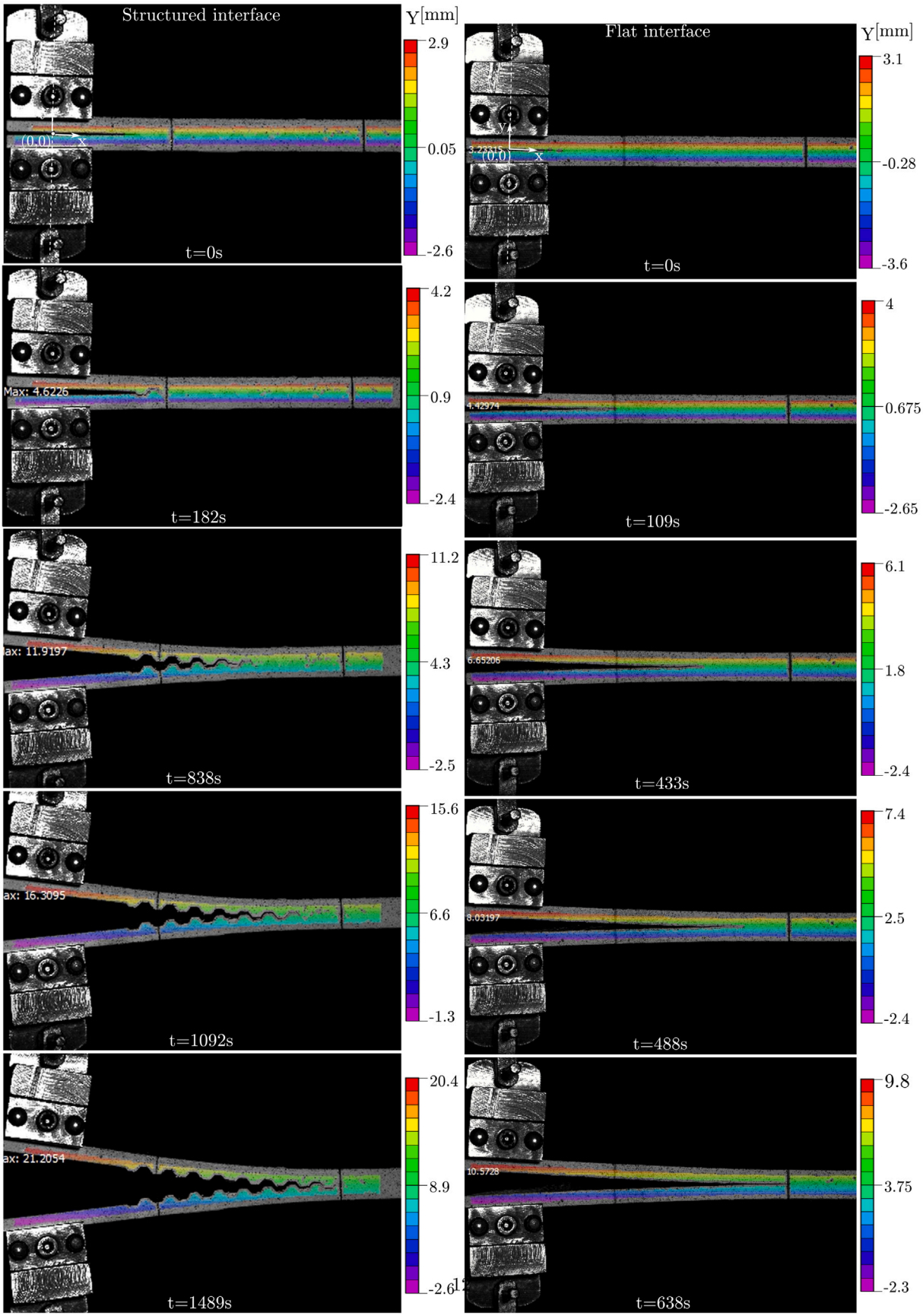

Fig. 8. DIC representing vertical displacement during crack propagation for structured (t_{1-1}) and flat (p_5) interfaces.

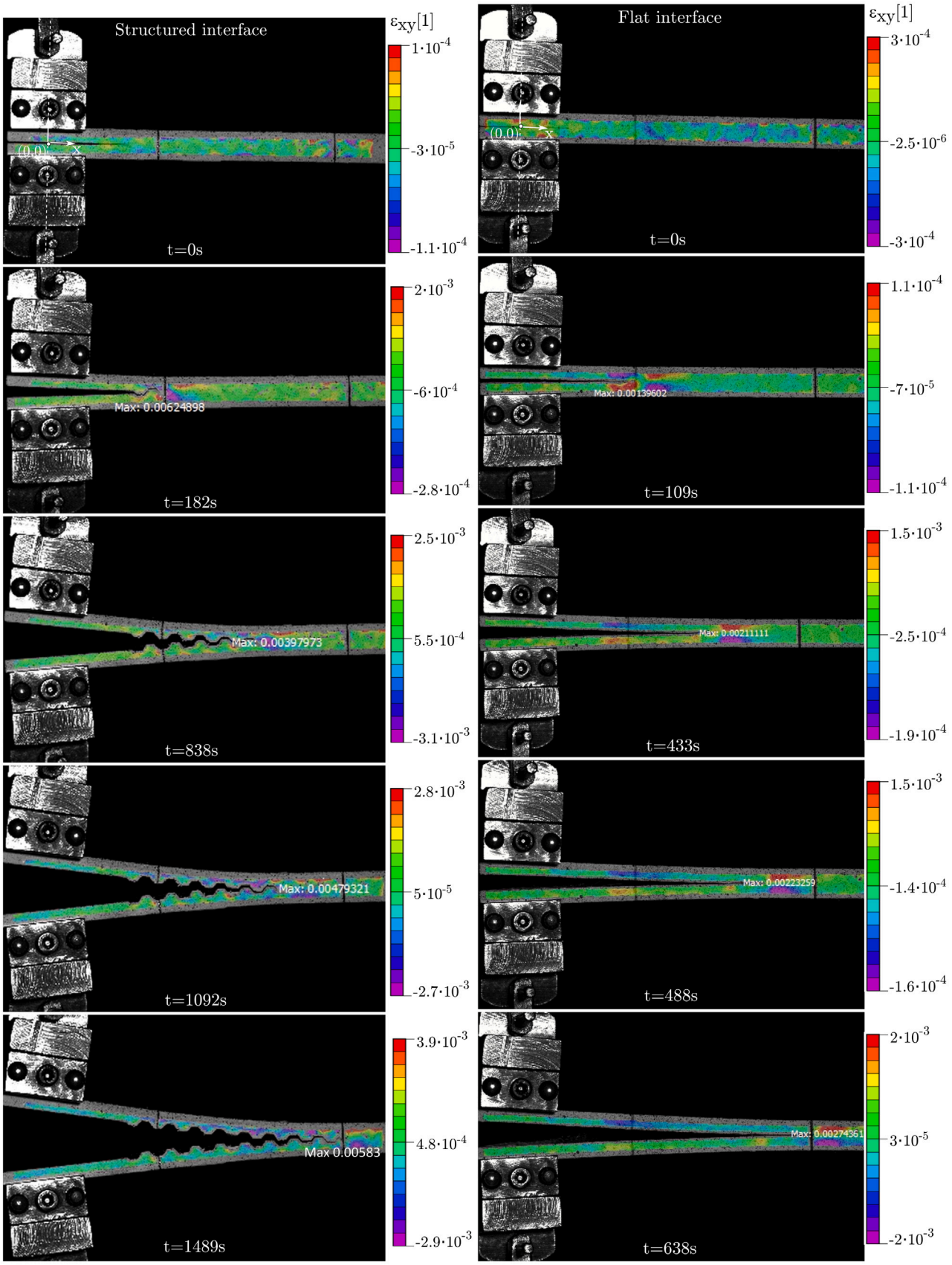

Fig. 9. DIC representing vertical strain during crack propagation for structured (t_{1-1}) and flat (p_5) interfaces.

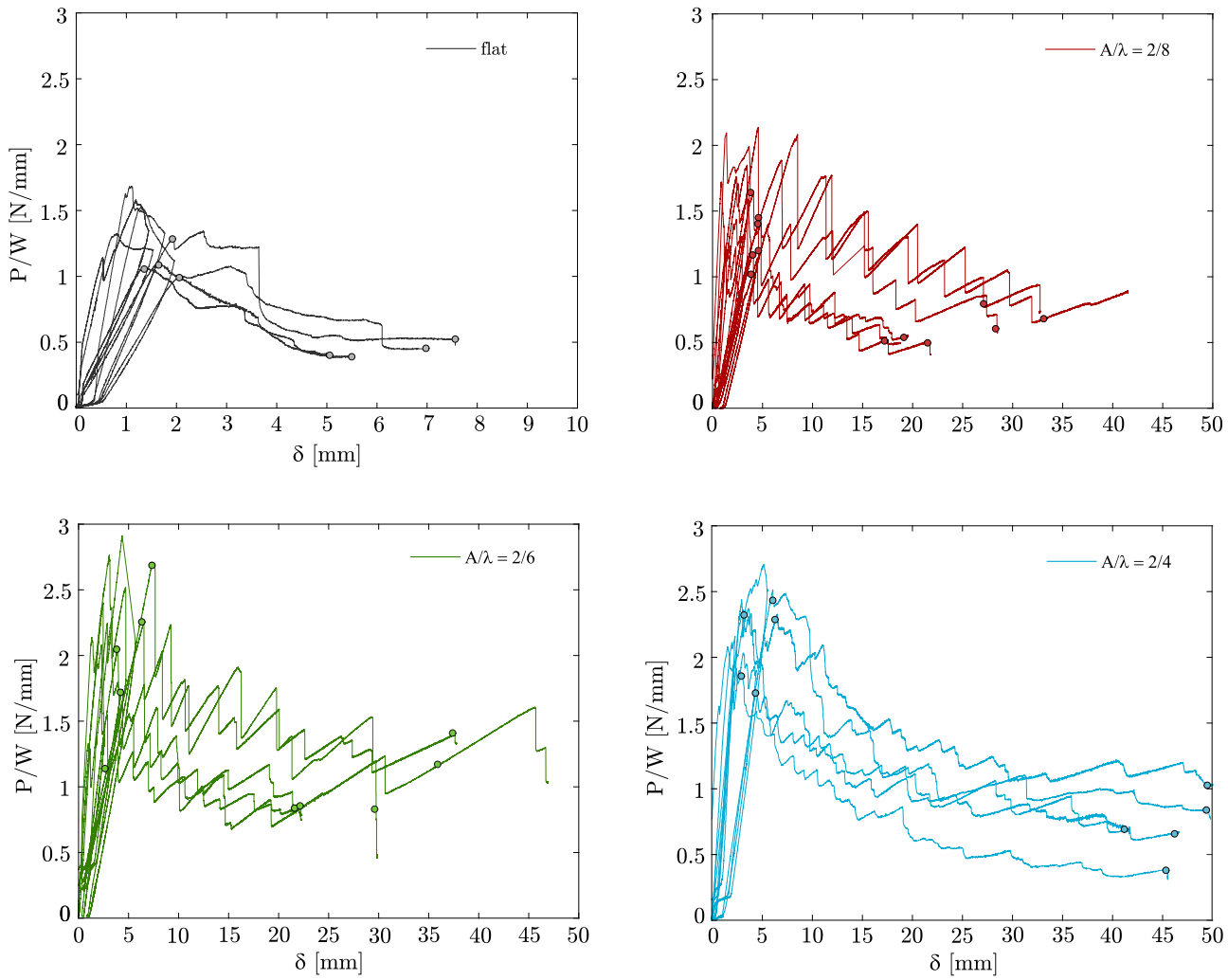

Fig. 10. Experimental load–displacement curves for patterns configurations with different aspect ratios, amplitude/wavelength 0-flat (black), 2/8 (red), 2/6 (green), 2/4 (blue).

calculated using the following expression:

$$G_{\mathrm{Ic}} = \frac{A}{aW} \tag{1}$$

where:

- G_{Ic} is the fracture toughness energy in J/m^2,
- A is the energy to achieve the total propagated crack length in J,
- a is the propagated crack length ($a = a_{i+n} - a_i$) in mm (final crack length minus initial crack length) and,
- W is the width of the specimen in mm.

However, DCB specimens with structured interfaces are prone to develop mixed mode fracture conditions at the interface. Accordingly, complying with the premise that energy is exclusively dissipated at the interface and for elastic deformation of the DCB beams, it is necessary to differentiate between two probable essential energy release rate values [12,14]:

(i) Considering the energy dissipated during the crack propagation when the crack is extended along the x-direction, defined by a_x in Fig. 3, obtaining the effective or apparent critical energy release rate, G^x_{Ic}, as follows:

$$G^{\mathrm{x}}_{\mathrm{Ic}} = -\frac{\partial \Pi_{\mathrm{f}}(a_{\mathrm{x}})}{\partial(W a_{\mathrm{x}})} \tag{2}$$

where $\Pi_f(a_x)$ is the energy dissipated during the crack propagation when the crack grows an area $dA_f = W da_x$.

(ii) Alternatively, considering the energy dissipated during the crack propagation when the crack is extended along the S-direction, designed by a_s in Fig. 3, obtaining the actual critical energy release rate, G^s_{Ic}, as follows:

$$G^{s}_{\mathrm{Ic}} = -\frac{\partial \Pi_f(a_s)}{\partial(W a_S)} \tag{3}$$

where $\Pi_f(a_s)$ is the energy dissipated during the crack propagation when the crack grows an area $dA_f = W da_s$ and s-direction is defined as the curvilinear pattern following the crack surface.

Particularly, the actual area formed by the crack growth ($W \times a_s$) and its projection on the horizontal plane ($W \times a_x$), between two different effective crack lengths (a_{x1} and a_{x2}), were employed to quantify such properties. Thus, for flat interfaces, this distance can be obtained by directly measuring the test specimen $a_x = a_s$. In contrast, for specimens with trapezoidal interfaces, the crack advance (a_s) may be defined as a function of interface geometrical parameters and the distance along the horizontal axis (x-axis): $a_s = a_s\ (a_x, A, \lambda)$.

The energy released in each configuration is represented by the enclosed area between the experimental curve and the straight lines from the origin to each marker, see Fig. 7.

Table 2 represents the effective and actual critical energy release rates, G^x_{Ic} and G^s_{Ic}, for the DCBs with trapezoidal and flat interfaces studied. It is observed that for higher A/λ ratios, higher improvements in fracture resistance are obtained with respect to flat interfaces, in

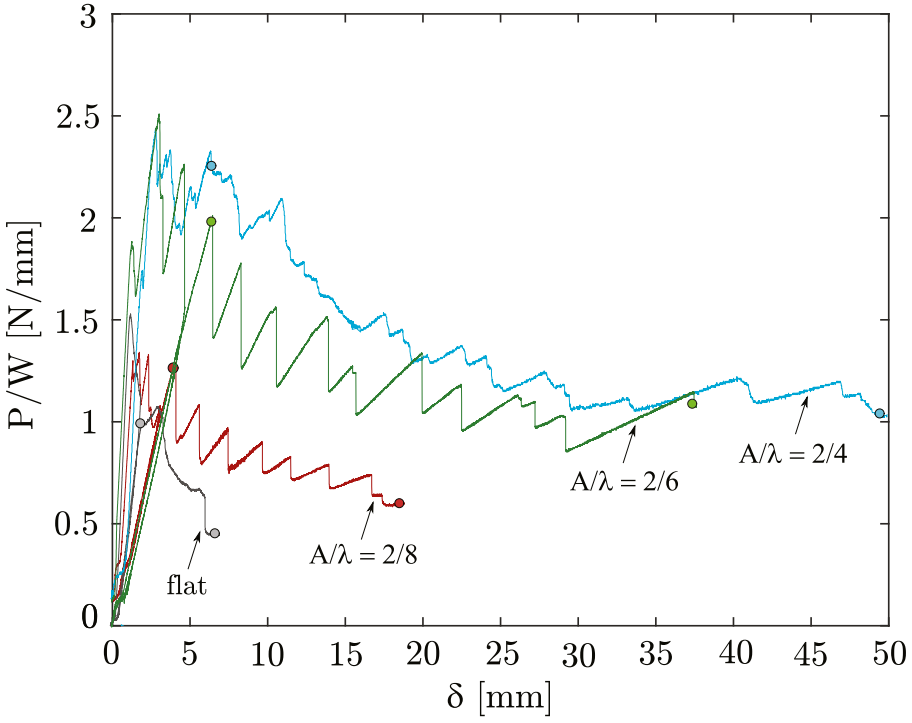

Fig. 11. Representative load–displacement curves for each patterns configurations with amplitude/wavelength 0-flat (black), 2/8 (red), 2/6 (green), 2/4 (blue).

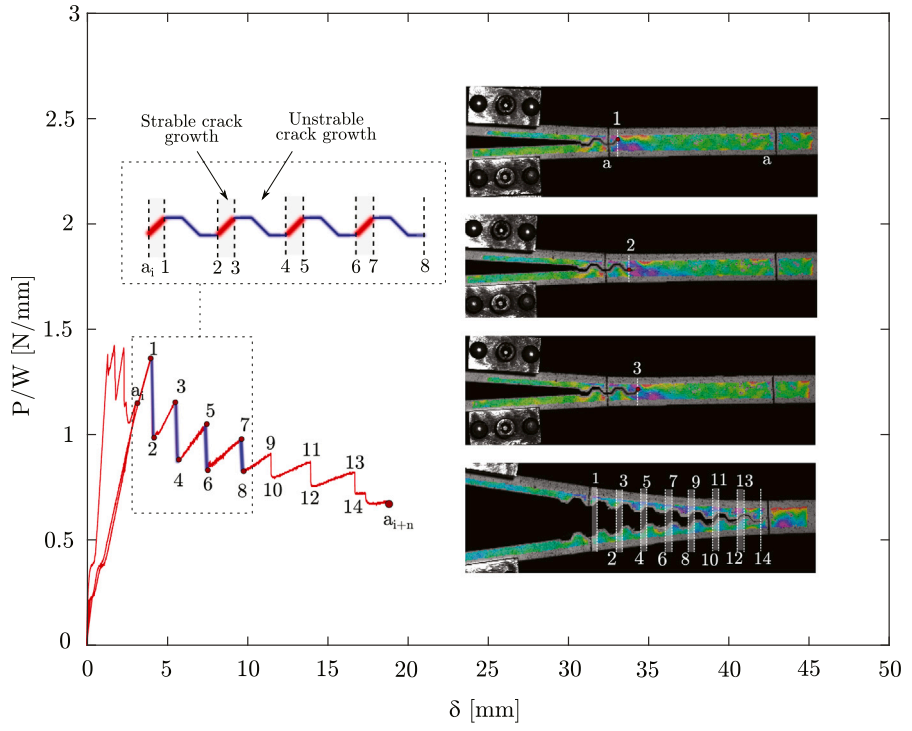

Fig. 12. A load–displacement for structured interface A/λ = 2/8. Sketch of stable/unstable crack growth in the structured profile. Series of dynamic images of crack propagation.

both G^x_{Ic} and G^s_{Ic}. This result implies that when A/λ increases, the contribution of fracture Mode II at the local crack tip becomes more significant. Indeed, since the findings of G^x_{Ic} can be understood as the critical energy release rate required to propagate a crack along the x-direction, greater values of A/λ result in the development of larger areas during the interface crack propagation.

Therefore, a significant improvement in fracture resistance performance is observed comparing the critical energy release rates for the proposed novel structured interface geometry with respect to flat interface DCBs. Compared to the reference values for flat interfaces, the most unfavorable configuration (A/λ = 2/8) experienced an increment of the corresponding effective critical energy release rate around 333%, whereas the actual critical energy release rate was increased around 259%. Although these improvements in the fracture resistance values are of considerable magnitude, the best configuration in these terms showed an increment of the effective and actual critical release rates

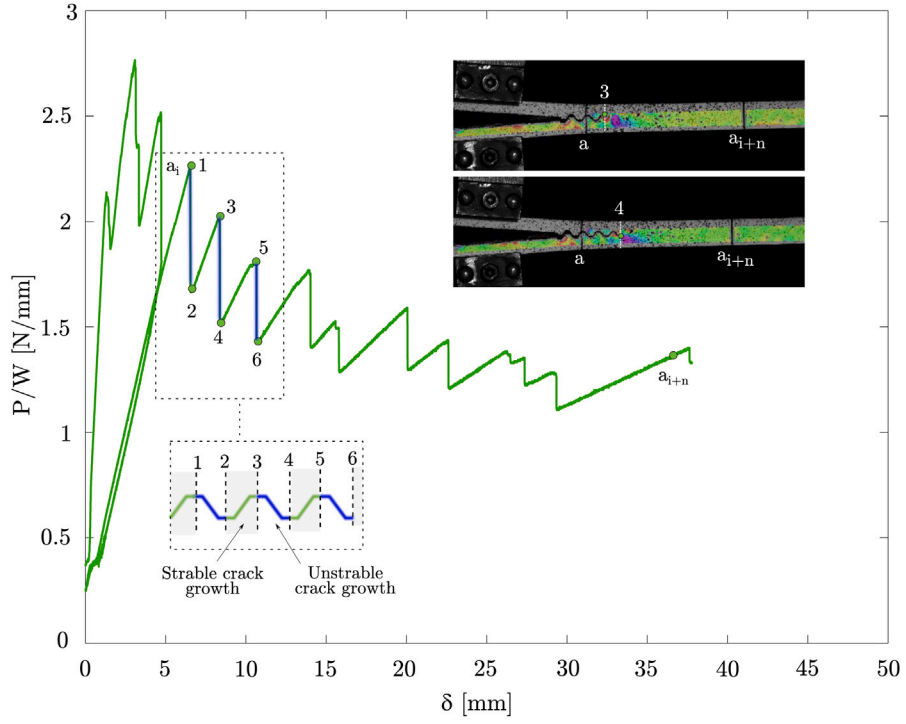

Fig. 13. A load–displacement for structured interface A/λ = 2/6. Sketch of stable/unstable crack growth in the structured profile. Series of dynamic images of crack propagation.

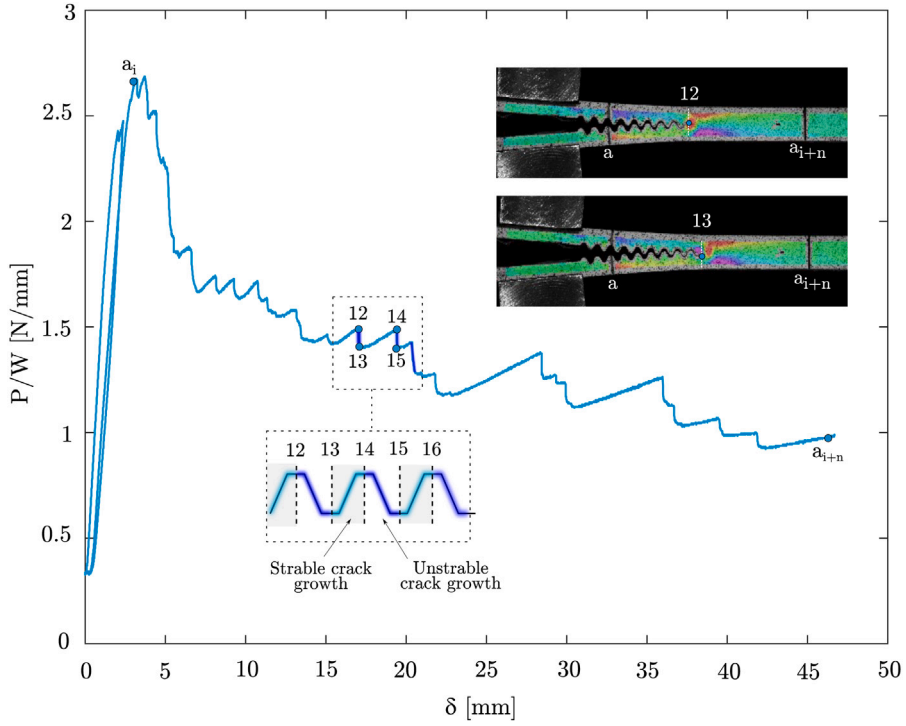

Fig. 14. A load–displacement for structured interface A/λ = 2/4. Sketch of stable/unstable crack growth in the structured profile. Series of dynamic images of crack propagation.

around 973% and 563%, respectively. These impressive data clearly reveal the potential crack resistance improvements that can be achieved by means of the production of specimens with structured interfaces (Table 3) (see Fig. 15).

Moreover, the failure observed in postmortem DCB specimens was adhesive failure. Similar observations were found by García-Guzmán et al. [14]. This could be due to the adhesive used is not the most appropriate to glue nylon.

4. Discussion

Since different printing directions as considered an important aspect, new designs of structured interface have been developed. Section 4 compares the fracture capabilities of structured interfaces printing in vertical direction versus horizontal direction, see Fig. 2.

The relative fracture energy for each configuration, structured interfaces with the fiber around the contour and structured interfaces

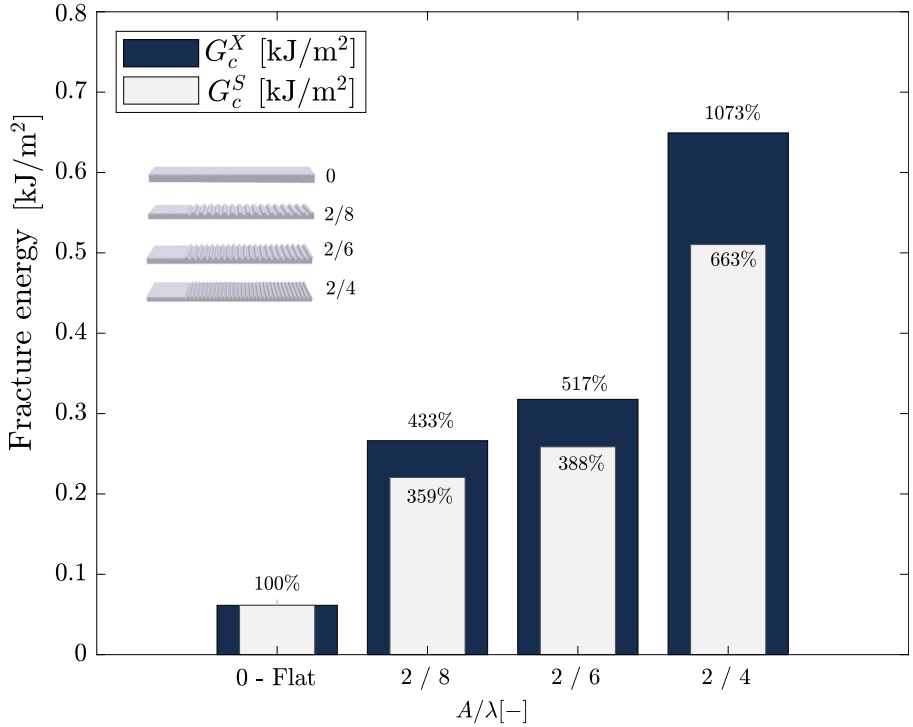

Fig. 15. Comparison G_c^x and G_c^s for structured design specimens printed in vertical direction with amplitude/wavelength: 0 (flat), 2/8, 2/6, 2/4. Comparison of structured specimens regard to flat case, $\frac{G_c^x}{G_{c|flat}^x}$ and $\frac{G_c^s}{G_{c|flat}^s}$ (reperensed in %).

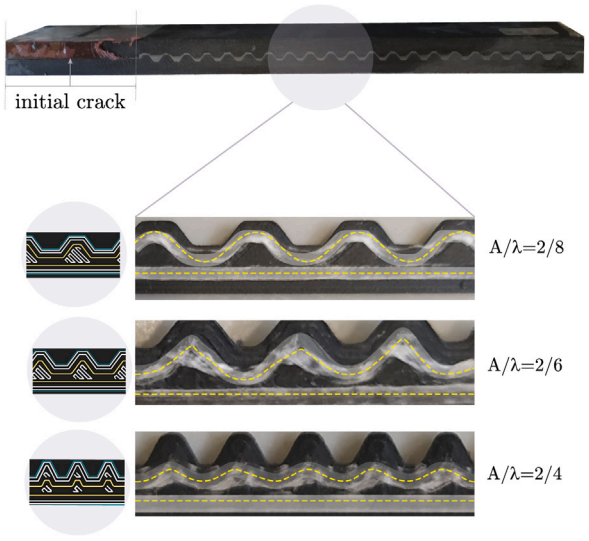

Fig. 16. Printing result of a fiberglass DCB specimen with structured interface A/λ = 2/6 mm printed in vertical direction. Direction of fiberglass around the profile for A/λ = 2/8, 2/6, 2/4.

Table 2
Effective fracture toughness, G_{Ic}^x, actual fracture toughness, G_{Ic}^s, and the ratio between effective and actual fracture toughness G_{Ic}^x/G_{Ic}^s.

Configuration	n°	A [mm]	λ [mm]	G_{Ic}^x [J/m^2]	G_{Ic}^s [J/m^2]
Flat	1	2	–	61.4	61.4
	2	2	–	53.1	53.1
	3	2	–	66.7	66.7
	4	2	–	64.4	64.4
t1	1	2	8	134.7	111.6
	2	2	8	196.1	162.4
	3	2	8	376.3	311.6
	4	2	8	137.6	114.0
	5	2	8	432.6	358.3
	6	2	8	320.2	265.3
t2	1	2	6	415.4	311.6
	2	2	6	450.2	337.7
	3	2	6	315.8	236.8
	4	2	6	174.4	130.7
	5	2	6	232.9	174.7
t3	1	2	4	608.9	376.3
	2	2	4	589.4	364.2
	3	2	4	668.9	413.4
	4	2	4	751.2	464.3
	5	2	4	676.0	417.8

with the fiber in the horizontal layers [14], is depicted in Figs. 17 and 18 when the crack is extended along the x-direction and along the S-direction, respectively.

These results reveal that specimens with the fiber placed around the profile presents a notably increase of fracture energy ratio than specimens with fiber placed only in the horizontal layers, becoming the increment of relative fracture energy ratio 217% for the best configuration and 118% for the most unfavorable configuration (see Table 4).

However, it is noted in Figs. 17 and 18 that the increment on relative fracture energy ratio in A/λ = 2/4 configuration is less significant

Table 3
Average G_{Ic}^x and G_{Ic}^s and comparison of improved structured design versus the flat case, $G_{Ic}^x/G_{Ic,flat}^x$ and $G_{Ic}^s/G_{Ic,flat}^s$.

$\frac{A}{\lambda}$	G_{Ic}^x [J/m^2]	G_{Ic}^s [J/m^2]	$\frac{G_{Ic}^x}{G_{Ic}^x\|flat}$	$\frac{G_{Ic}^s}{G_{Ic}^s\|flat}$
0 flat	61.40	61.40	1	1
2/8	266.25	220.55	4.33	3.59
2/6	317.74	238.3	5.17	3.88
2/4	658.88	407.16	10.73	6.63

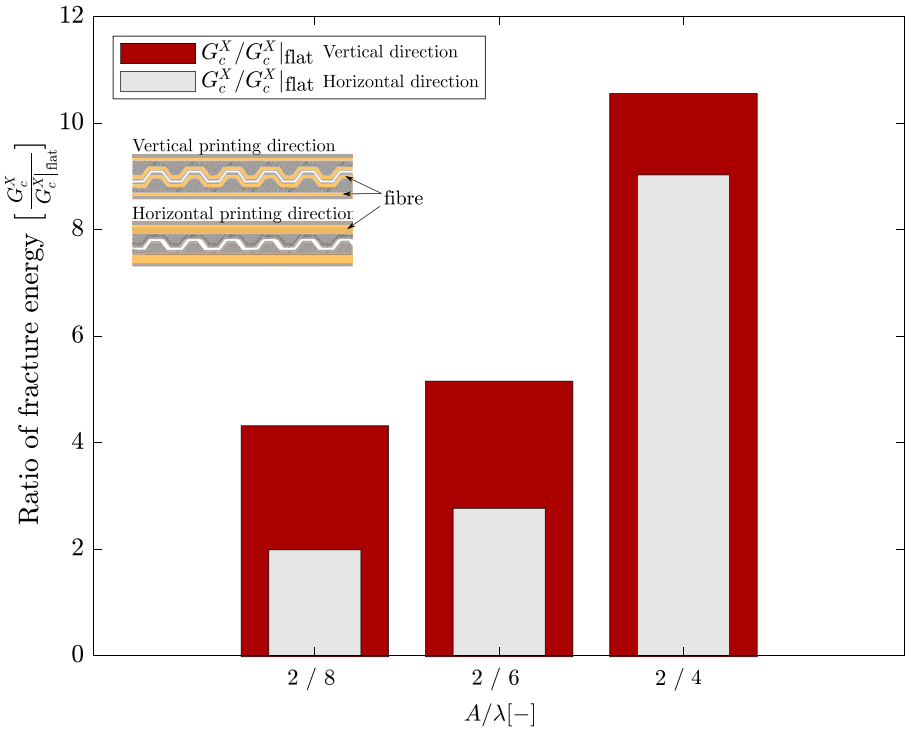

Fig. 17. Relative comparison of fracture energy ratio when the crack is extended along the x-direction in improved design with fiber around the profile printed in the vertical direction with a configuration designed in [14] printed in the horizontal direction.

Table 4
Comparison of structured design printing in vertical direction versus structured design printing in horizontal direction, $\frac{G_{Ic|\text{vertical}}^x/G_{Ic|\text{flat}}^x}{G_{Ic|\text{horizontal}}^x/G_{Ic|\text{flat}}^x}$.

$\frac{A}{\lambda}$	$\frac{G_c^x}{G_{c\|\text{flat}}^x}$(vert.dir.)	$\frac{G_c^x}{G_{c\|\text{flat}}^x}$(horiz.dir.)	$\frac{G_c^x/G_{c\|\text{flat}}^x(\text{vert.dir.})}{G_c^x/G_{c\|\text{flat}}^x(\text{horiz.dir.})}$
2/8	4.33	1.99	2.17
2/4	5.17	2.72	1.90
2/4	10.73	9.03	1.18

for A/λ = 2/8 and 2/6 designs which were around double compared to García-Guzmán et al. [14]. When the wavelength is shorter, it is more difficult for the printer to deposit the fiber on the contour. As a result, the A/λ = 2/4 configuration, with a shorter wavelength, made it less accessible for the 3D printer to deposit the fiber on the profile in the same manner as it did for A/λ = 2/8 and 2/6 geometries (Fig. 16). Consequently, A/λ = 2/4 configuration is more similar to García-Guzmán et al. [14], which is reflected in a lower improvement in the fracture energy ratio capabilities of this work in comparison to García-Guzmán et al. [14].

5. Conclusions

Structural materials found in nature include interfaces with complex geometries, which increase the apparent fracture toughness of these materials. The advent of current Additive Layer Manufacturing (ALM) techniques opens a new paradigm in terms of interface design, allowing for the reproduction of geometric definitions inspired by nature.

The objective motivating this study was to evaluate the different 3D printing methods on the fracture performance in DCB composite specimens including structured interfaces fiber-reinforced 3D printed. This could be particularly relevant for practical biomimetic designs.

For this purpose an experimental study of crack propagation along structured patterned in DCB was presented. Four different structured patterns with different aspect ratios, A/λ = 2/8, 2/6, 2/4, 0 (flat) were tested. The DIC system was employed in this investigation to describe the stable/unstable crack growth.

Experimental evidence shows that alternative structured designs have a significant increase in fracture toughness when compared to previous structured interface profiles. Such enhancement of the effective critical fracture toughness increases with the ratio A/λ.

The present investigation pinpoints important aspects concerning the 3D printing production options for fiber reinforced composites that will be exploited in forthcoming applications such as runout specimens, single-lap joints, mixed-mode fracture tests, among others.

CRediT authorship contribution statement

M.T. Aranda: Conceptualization, Design, Analysis, Writing, Writing – review & editing. **J. Reinoso:** Conceptualization, Design, Analysis, Writing, Writing – review & editing. **I.G. García:** Conceptualization, Design, Analysis, Writing, Writing – review & editing.

Declaration of competing interest

The authors declare that they have no known competing financial interests or personal relationships that could have appeared to influence the work reported in this paper.

Data availability

Data will be made available on request.

Acknowledgments

This investigation was supported by Consejería de Economía y Conocimiento, Junta de Andalucía, and European Regional Development Fund (Project P20-00595).

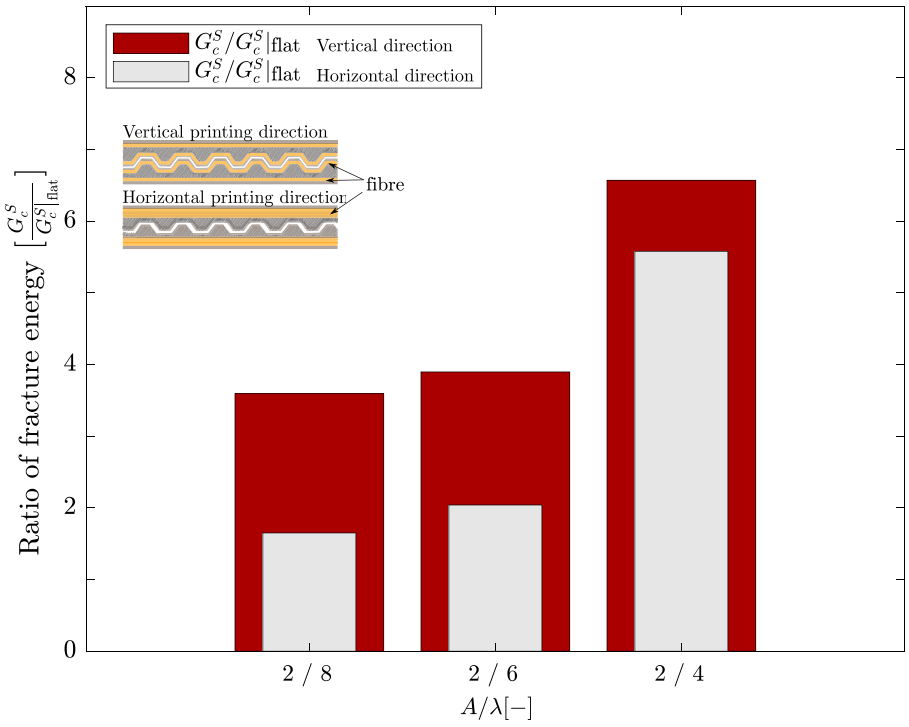

Fig. 18. Relative comparison of fracture energy ratio when the crack is extended along the S-direction in improved design with fiber around the profile printed in the vertical direction with a configuration designed in [14] printed in the horizontal direction.

References

[1] M. Alam, J. Parmigiani, J. Kruzic, An experimental assessment of methods to predict crack deflection at an interface, Eng. Fract. Mech. 181 (2017) 116–129.

[2] B. Sundaram, H. Tippur, Dynamics of crack penetration vs.branching at a weak interface: An experimental study, Mech. Phys. Solids 96 (2016) 312–333.

[3] M. Aranda, I. García, J. Reinoso, V. Mantič, M. Paggi, Crack arrest through branching at curved weak interfaces: An experimental and numerical study, Theor. Appl. Fract. Mech. 105 (2020) 1–14.

[4] M. Aranda, I. García, J. Reinoso, V. Mantič, Experimental evaluation of the similarity in the interface fracture energy between pmma/epoxy/pmma and pmma/epoxy joints, Eng. Fract. Mech. 259 (2022) 108076.

[5] F. Libonati, M. Buehler, Advanced structural materials by bioinspiration: Advanced structural materials by bioinspiration, Adv. Energy Mater. 19 (2017) 1600787.

[6] R. Rabiei, S. Bekah, F. Barthelat, Failure mode transition in nacre and bone-like materials, Acta Biomater. 6 (10) (2010) 4081–4089.

[7] F. Barthelat, Architectured materials in engineering and biology: fabrication, structure, mechanics and performance., Int. Mater. Rev. 60 (8) (2015) 413–430.

[8] Y. An, J. Han, X. Zhang, W. Han, Y. Cheng, P. Hu, G. Zhao, Bioinspired high toughness graphene/ZrB2 hybrid composites with hierarchical architectures spanning several length scales, Carbon 107 (2016) 209–216.

[9] J. Dunlop, P. Fratzl, Multilevel architectures in natural materials, Scr. Mater. 68 (1) (2013) 8–12.

[10] N. Lee, M. Horstemeyer, H. Rhee, B. Nabors, J. Liao, N. Williams, Hierarchical multiscale structure–property relationships of the red-bellied woodpecker (melanerpes carolinus) beak, J. R. Soc. Interface 11 (96) (2014) 014009.

[11] M. Mirkhalaf, A. Khayer Dastjerdi, F. Barthelat, Overcoming the brittleness of glass through bio-inspiration and micro-architecture, Nature Commun. 5 (2014) 3166.

[12] F. Cordisco, P. Zavattieri, L. Hector, B. Carlson, Mode I fracture along adhesively bonded sinusoidal interfaces, Int. J. Solids Struct. 83 (2016) 45–64.

[13] I. Malik, M. Mirkhalaf, F. Barthelat, Bio-inspired "jigsaw"-like interlocking sutures: Modeling, optimization, 3d printing and testing, J. Mech. Phys. Solids 102 (2017) 224–238.

[14] L. García-Guzmán, L. Távara, J. Reinoso, J. Justo, F. París, Fracture resistance of 3D printed adhesively bonded DCB composite specimens using structured interfaces: Experimental and theoretical study, Compos. Struct. 188 (2017) 173–184.

[15] L.S. Dimas, M. Buehler, Modeling and additive manufacturing of bio-inspired composites with tunable fracture mechanical properties, Soft Matter 10 25 (2014) 4436–4442.

[16] U.G. Wegst, H. Bai, E. Saiz, A. Tomsia, R. Ritchie, Bioinspired structural materials, Nature Mater. 14 (2015) 23–36.

[17] Z. Jia, L. Wang, 3D printing of biomimetic composites with improved fracture toughness, Acta Mater. 173 (2019) 61–73.

[18] A. Srivastava, S. Osovski, A. Needleman, Engineering the crack path by controlling the microstructure, J. Mech. Phys. Solids 100 (2017) 1–20.

[19] W. Zhang, C. Wu, C. Zhang, Z. Chen, Microstructure and mechanical property of turtle shell, Theor. Appl. Mech. Lett. 2 (1) (2012) 014009.

[20] F. Barthelat, M. Mirkhalaf, A.K. Dastjerdi, Method for increasing toughness and resistance to impact of material, involves engineering predetermined property of material by introduction of weak interfaces into materials, 2015, Patent Number: CA2883427-A1 US2015274587-A1.

[21] G. Álvarez, A. Zafra, F. Belzunce, C. Rodríguez, Hydrogen embrittlement testing procedure for the analysis of structural steels with Small Punch Tests using notched specimens, Eng. Fract. Mech. 253 (2021) 107906.

[22] E. Lin, Y. Li, C. Ortiz, M. Boyce, 3D printed, bio-inspired prototypes and analytical models for structured suture interfaces with geometrically-tuned deformation and failure behavior, J. Mech. Phys. Solids 73 (2014) 166–182.

[23] M. Sánchez, S. Cicero, S. Arrieta, V. Martínez, Fracture load predictions in additively manufactured ABS U-notched specimens using average strain energy density criteria., Materials (Basel) 23 (15(7)) (2022) 2372.

[24] B. Ameri, F. Taheri-Behrooz, M. Aliha, Evaluation of the geometrical discontinuity effect on mixed-mode I/II fracture load of FDM 3D-printed parts, Theor. Appl. Fract. Mech. 113 (2021) 102953.

[25] S. Shahbaz, M. Ayatollahi, M. Petru, A. Torabi, U-notch fracture in additively manufactured ABS specimens under symmetric three-point bending, Theor. Appl. Fract. Mech. 119 (2022) 103318.

[26] A.R. Dusane, P.R. Budarapu, A.K. Pradhan, S. Natarajan, J. Reinoso, M. Paggi, Simulation of bridging mechanisms in complex laminates using a hybrid PF-CZM method, Mech. Adv. Mater. Struct. (2022) 1–29.

[27] S. Sharma, R. Awasthi, Y.e.a. Sastry, Physics-informed neural networks for estimating stress transfer mechanics in single lap joints, J. Zhejiang Univ. Sci. A 22 (2021) 621–631.

[28] P. Budarapu, S. Thakur, S. Kumar, M. Paggi, Micromechanics of engineered interphases in nacre-like composite structures, Mech. Adv. Mater. Struct. 28 (22) (2021) 2327–2342.

[29] P. Budarapu, S. Kumar, B. Gangadhara Prusty, M. Paggi, Stress transfer through the interphase in curved-fiber pullout tests of nanocomposites, Composites B 165 (2019) 417–434.

[30] J. Reinoso, A. Blázquez, L. Távara, F. París, C. Arellano, Damage tolerance of composite runout panels under tensile loading, Composites B 96 (2016) 79–93.

[31] J. Reinoso, A. Blázquez, A. Estefani, F. París, J. Cañas, A composite runout specimen subjected to tension–compression loading conditions: Experimental and global–local finite element analysis, Compos. Struct. 101 (2013) 274–289.

[32] J. Reinoso, A. Blázquez, A. Estefani, F. París, J. Cañas, E. Arévalo, F. Cruz, Experimental and three-dimensional global-local finite element analysis of a composite component including degradation process at the interfaces, Composites B 43 (4) (2012) 1929–1942.
[33] F.J. Honorato Ruiz, et al., Optimized stringer run-out zone in aircraft componets, 2013, Patent U.S. 20130101801A1.
[34] C. García Nieto, F.J. Honorato Ruiz, Composite structure for an aircraft and manufacturing method thereof, 2014, European Patent EP2799220A1.
[35] A. Blazquez, J. Reinoso, F. Parıs, A. Estefani, E. Arévalo, F. Cruz, Analysis of a stringer run-out concept including damage initiation and evolution at the interfaces, in: ECCM15-15TH European Conference on Composite Materials, Venice, Italy, 2012.
[36] C. Ridgard, Out of autoclave composite technology for aerospace, defense and space structures, in: International SAMPE Symposium and Exhibition, Vol. 54, 2009, p. 15.
[37] S.L. Agius, K. Magniez, B. Fox, Cure behaviour and void development within rapidly cured out-of-autoclave composites, Composites B 47 (2013) 230–237.
[38] J. Justo, L. Távara, L. García-Guzmán, F. París, Characterization of 3D printed long fibre reinforced composites, Compos. Struct. 185 (2018) 537–548.
[39] R.J. Nash, Y. Li, Experimental and numerical analysis of 3D printed suture joints under shearing load, Eng. Fract. Mech. 253 (2021) 107912.
[40] AITM1-0053, Carbon Fibre Reinforced Plastics. Determination of Mode I Fracture Toughness Energy of Bonded Joints. G_{1C} Test, Standard Issue 6, Technical report, Airbus, 31707 Blagnac Cedex France, 2015, pp. 1–29.
[41] ISO Central Secretary, fibre-Reinforced Plastic Composites – Determination of Mode I Interlaminar Fracture Toughness, GIC, for Unidirectionally Reinforced Materials, Standard, Technical report, 2001.
[42] M. Mudarra Acebedo, Puesta a Punto y Caracterización de Probetas de Material Compuesto Fabricadas con un Sistema de Impresión 3D. (Trabajo fin de Grado Inédito), Universidad de Sevilla, 2021.
[43] G. Bresson, J. Jumel, M.E.R. Shanahan, P. Serin, Statistical aspects of the mechanical behaviour a paste adhesive, Int. J. Adhes. Adhes. 79 (2013) 40–70.